Precise Control of Phase Separation Enables 12% Efficiency in All Small Molecule Solar Cells

Haijun Bin, Indunil Angunawela, Beibei Qiu, Fallon J. M. Colberts, Mengmeng Li, Matthew J. Dyson, Martijn M. Wienk, Harald Ade,* Yongfang Li,* and René A. J. Janssen*

Compared to conjugated polymers, small-molecule organic semiconductors present negligible batch-to-batch variations, but presently provide comparatively low power conversion efficiencies (PCEs) in small-molecular organic solar cells (SM-OSCs), mainly due to suboptimal nanomorphology. Achieving precise control of the nanomorphology remains challenging. Here, two new small-molecular donors H13 and H14, created by fluorine and chlorine substitution of the original donor molecule H11, are presented that exhibit a similar or higher degree of crystallinity/aggregation and improved open-circuit voltage with IDIC-4F as acceptor. Due to kinetic and thermodynamic reasons, H13-based blend films possess relatively unfavorable molecular packing and morphology. In contrast, annealed H14-based blends exhibit favorable characteristics, i.e., the highest degree of aggregation with the smallest paracrystalline π–π distortions and a nanomorphology with relatively pure domains, all of which enable generating and collecting charges more efficiently. As a result, blends with H13 give a similar PCE (10.3%) as those made with H11 (10.4%), while annealed H14-based SM-OSCs have a significantly higher PCE (12.1%). Presently this represents the highest efficiency for SM-OSCs using IDIC-4F as acceptor. The results demonstrate that precise control of phase separation can be achieved by fine-tuning the molecular structure and film formation conditions, improving PCE and providing guidance for morphology design.

1. Introduction

Bulk-heterojunction (BHJ) organic solar cells (OSCs) composed of *p*-type conjugated polymers or small molecule donors blended with *n*-type conjugated polymers or small molecule acceptors have attracted widespread interest over the last three decades, primarily because of attractive properties, such as light weight, flexibility, and compatibility with large area manufacturing techniques in combination with increasing efficiencies.[1–3] OSCs are generally classified as either all-polymer solar cells (all-PSCs, both donor and acceptor are polymers), polymer solar cells (PSCs, donor or acceptor is polymeric), or all small-molecule organic solar cells (SM-OSCs, both donor and acceptor are small molecules). Driven by novel photovoltaic materials and improved device optimization, power conversion efficiencies (PCEs) have recently surpassed 17% for single junction PSCs.[4–7] Although this value is less than what competing photovoltaic technologies based on silicon or perovskite achieve, the unique attributes of OSCs

Dr. H. Bin, Dr. M. Li, Dr. M. J. Dyson, Dr. M. M. Wienk, Prof. R. A. J. Janssen
Molecular Materials and Nanosystems and Institute for Complex Molecular Systems
Eindhoven University of Technology
P.O. Box 513, Eindhoven 5600 MB, The Netherlands
E-mail: r.a.j.janssen@tue.nl

I. Angunawela, Prof. H. Ade
Department of Physics and Organic and Carbon Electronics Lab (ORaCEL)
North Carolina State University
Raleigh, NC 27695, USA
E-mail: hwade@ncsu.edu

B. Qiu, Prof. Y. Li
Beijing National Laboratory for Molecular Sciences, CAS Key Laboratory of Organic Solids, Institute of Chemistry
Chinese Academy of Sciences
Beijing 100190, China
E-mail: liyf@iccas.ac.cn

Dr. F. J. M. Colberts
Energy Engineering
Zuyd University of Applied Sciences
Nieuw Eyckholt 300, Heerlen 6419 DJ, The Netherlands

Dr. M. Li, Prof. R. A. J. Janssen
Dutch Institute for Fundamental Energy Research
De Zaale 20, Eindhoven 5612 AJ, The Netherlands

Dr. M. Li
Key Laboratory of Microelectronic Devices and Integrated Technology
Institute of Microelectronics
Chinese Academy of Sciences
Beijing 100029, China

**ADVANCED
SCIENCE NEWS**

www.advancedsciencenews.com

**ADVANCED
ENERGY
MATERIALS**

www.advenergymat.de

and the declining efficiency gap contribute to the application potential of OSCs. The substantial PCE enhancement in recent years mainly originates from the development of new narrow bandgap nonfullerene acceptors (NFAs), which provide broad absorption spectra, energy levels suitable for charge separation, and high electron mobility.[5–11] NFAs are commonly matched with wide bandgap polymer donors to obtain high efficiency OSCs.[9–11] However, due to synthetic complexity, batch-to-batch variations of polymer donors often lead to reduced reproducibility of device performance, hindering the commercialization of OSCs.[12–15]

Small molecule donors offer a possible solution to this problem. Unlike conjugated polymers, small-molecule organic semiconductors have a well-defined structure and feature negligible batch-to-batch variations after purification,[14–19] while large-scale synthesis is facilitated by well-defined catalyst requirements. Due to the uniform molecular structure of its components, SM-OSCs offer high reproducibility in device fabrication and the possibility of vapor deposition, which can enhance stability.[20,21] Despite these apparent advantages, many researchers focus on PSCs, because they feature higher PCEs, exceeding 17% recently, than SM-OSCs for which the maximum PCE is presently 15%.[16] As a consequence, compared to the large variety of high-performance polymer donor materials and associated efficient PSCs, the development of small molecule donor materials and their performance in SM-OSCs is somewhat neglected but warrants more attention. The comparatively low efficiency of SM-OSCs is widely attributed to a suboptimal phase separation between the donor and acceptor, likely due to the increased configurational entropy of SM-OSCs and thus much higher critical Flory–Huggins parameter (χ) compared to PSCs, which results in a lower short-circuit current density (J_{sc}) and fill factor (FF).[22–24] Molecular packing characteristics of the donor and acceptor molecules, i.e., degree of crystallinity/aggregation, texture, and coherence length,[25] can enhance charge transport, but also affect the characteristic domain size of the phase separation in the blend, which should be fine enough to enable exciton dissociation and coarse enough to facilitate charge transport. Moreover, the presence of two components and their intermolecular interactions will impact the molecular packing of the small molecules and morphology evolution during film formation. Hence, control of the phase separation and morphology in the active layer of SM-OSCs is challenging.
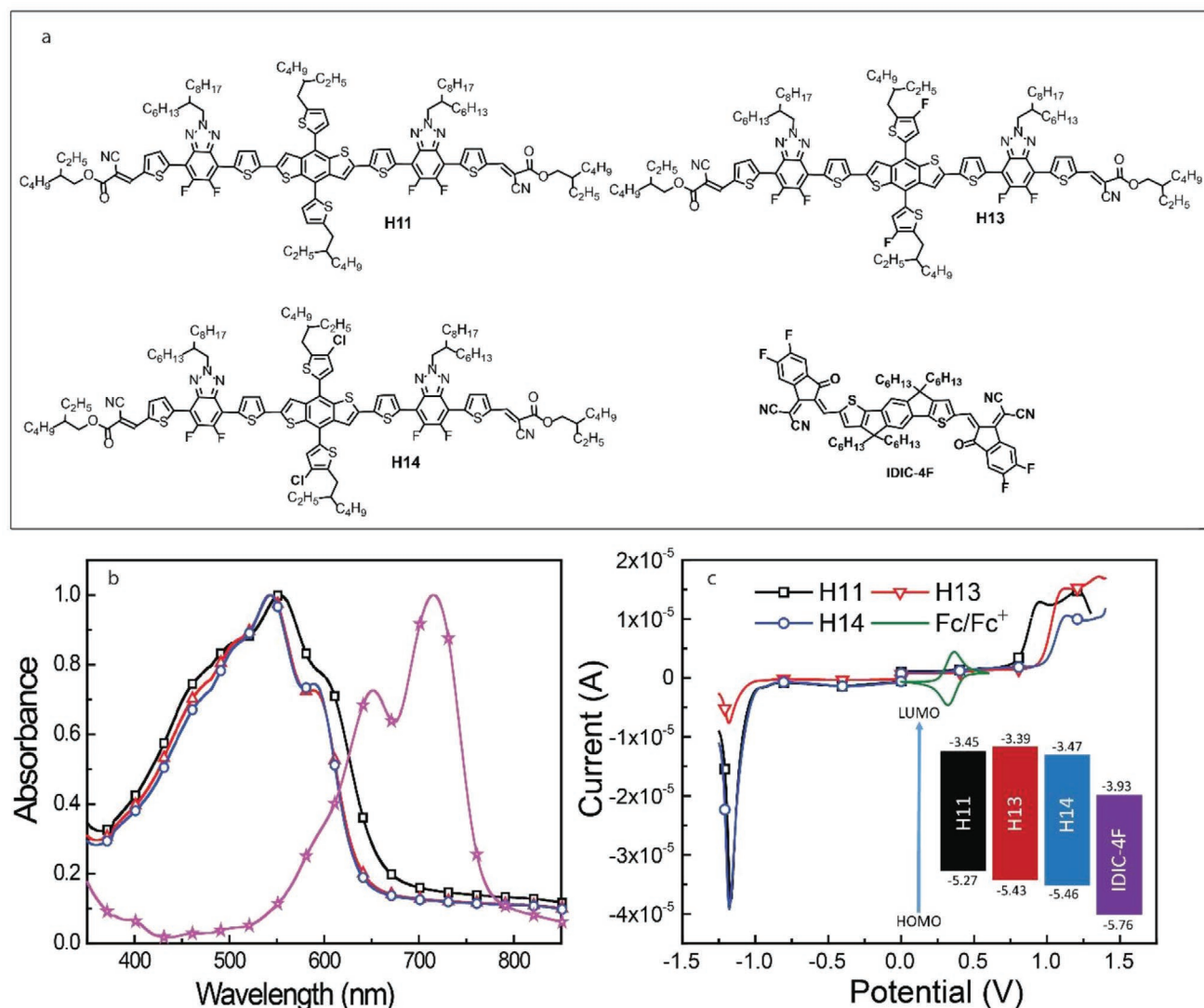
Given the dependence of the PCE on phase separation, achieving precise control is crucial. The phase separation of the active layer can generally be manipulated by the design of the molecular structure and by optimizing the device processing, e.g., by using cosolvents, thermal annealing, or solvent vapor annealing.[17,18,23,26] An important example of the design of the molecular structure is fluorine and chlorine substitution, which along with adjusting the energy levels also influences the phase separation and molecular assembly by strengthening intermolecular interactions. Indeed, such substitution has widely been reported to increase PCE in PSCs.[27–31] Previously we reported a small-molecule donor **H11**, based on an electron-rich benzodithiophene (BDT) central donor unit sandwiched by two adjacent electron-deficient difluorobenzotriazole units, which showed promising photovoltaic performance with IDIC as

acceptor.[24] In this work, based on **H11**, we develop two new small-molecule donors **H13** and **H14** by introducing either two F or two Cl atoms on the conjugated side chains of the BDT unit. Our aim is to downshift the energy levels and systematically study the effects of F and Cl substitution on the electronic properties of the molecules and on the morphological properties of the pristine materials and their blends with IDIC-4F as acceptor.[32] Pertinent to the inherent challenges in increasing efficiency of SM-OSCs via achieving an optimal morphology, we aim to decouple the influence of halogenation on intrinsic molecular properties from the active layer phase separation, and thus develop guidelines for achieving higher PCEs by adjusting the structure of the small-molecule donor. We find that after thermal annealing the PCEs of the SM-OSCs with **H11**, **H13**, and **H14** as donor and IDIC-4F as acceptor reach 10.4%, 10.3%, and 12.1%. Compared to **H11** without halogen atoms, the fluorinated **H13**-based cell shows a similar performance, while the chlorinated **H14**-based cell shows a significant increase. We demonstrate that the prime reason for this difference is in the blend film morphology, whose complexity requires consideration of the degree of crystallinity/aggregation, texture, and coherence length for the donor and acceptor, as well as domain size and domain purity, which in turn are driven by molecular interactions. **H13** and IDIC-4F are more miscible than the other two blends, leading to a suboptimal phase separation that counteracts the increased open-circuit voltage achieved by lowering the energy levels. In contrast, **H14** blends exhibit the most appropriate phase separation with IDIC-4F, featuring a high degree of aggregation for both donor and acceptor, favorable texture and domain size and purity characteristics that improve with thermal annealing and support the high FF. The different molecular interactions of the three donors induce different film morphologies, which lead to a difference in performance.

2. Results and Discussion

The chemical structures of **H11**, **H13**, **H14**, and IDIC-4F are shown in **Figure 1**a and the synthetic route to the donors is depicted in Scheme S1 (Supporting Information). The small-molecule donors were obtained in a palladium-catalyzed Stille-coupling reaction with high yield. The details of the synthesis procedures and molecular characterization are described in the Supporting Information. All three donors show good solubility in dichloromethane and chloroform, ensuring straightforward purification and solution processing of devices.

The thin film optical absorption spectra of the three small-molecule donors and IDIC-4F are shown in Figure 1b. **H11** shows a slightly redshifted absorption compared to **H13** and **H14**, attributed to the introduction of the electronegative halogens that reduce the intramolecular charge transfer absorption in **H13** and **H14**. All three molecules exhibit an absorption band between 400 and 650 nm. Their optical bandgaps estimated from the absorption onset are 1.88, 1.93, and 1.94 eV, respectively (Table S1, Supporting Information). The IDIC-4F acceptor absorbs between 550 and 800 nm, with an optical bandgap of 1.61 eV. Hence, the donors and IDIC-4F have largely complementary absorption between 400 and 800 nm, which is a prerequisite for a high J_{sc}.

ADVANCED
SCIENCE NEWS
www.advancedsciencenews.com

ADVANCED
ENERGY
MATERIALS
www.advenergymat.de

Figure 1. a) The chemical structures of **H11**, **H13**, **H14**, and IDIC-4F. b) Optical absorption spectra of **H11** (black line), **H13** (red line), **H14** (blue line), and IDIC-4F (magenta line) in thin films. b) Square-wave voltammograms of **H11**, **H13**, and **H14** on a platinum wire in 0.1 mol L^{-1} Bu$_4$NPF$_6$ acetonitrile solutions at a scan rate of 20 mV s^{-1}. Potentials are against Ag/AgCl. The inset shows the energy level diagram.

The energy levels of **H11**, **H13**, and **H14** were determined by square-wave voltammetry in which the molecules were present as thin films on a platinum wire (Figure 1c). By taking the onsets of the oxidation and reduction waves and applying $E_{HOMO/LUMO} = -q(E_{ox/red} - E_{1/2}(Fc/Fc^+) + 4.8)$ (eV), the energies of highest occupied molecular orbital (HOMO) and lowest unoccupied molecular orbital (LUMO) have been determined to be −5.27/−3.45 eV for **H11**, −5.43/−3.39 eV for **H13**, and −5.46/−3.47 eV for **H14**. Introducing electronegative halogens thus reduces the HOMO energies. **H14** has the deepest HOMO energy, implying that in an SM-OSCs **H14** is expected to have the highest V_{oc}. Since the HOMO/LUMO of IDIC-4F are located at −5.76/−3.93 eV, the HOMO and LUMO offsets of the three donors and IDIC-4F are sufficient to facilitate exciton dissociation and charge separation.

The photovoltaic properties of the three donors were investigated by fabricating BHJ SM-OSCs with a conventional indium tin oxide (ITO)/poly(3,4-ethylenedioxythiophene)-poly(styrenesulfonate) (PEDOT:PSS)/active layer/PDINO/Al device structure. Processing conditions, such as the donor:acceptor weight ratio, temperature, and time for thermal annealing, cosolvents, and solvent vapor annealing conditions were carefully optimized to maximize the PCE (detailed device optimization parameters are provided in Figures S1–S3 and Tables S2–S8, Supporting Information). The best conditions found for active layer formation are a donor:acceptor weight ratio of 2:1 (for **H13** this is 1.5:1), a total donor/acceptor concentration of 20 mg mL^{-1} in chloroform, spin coating at 2500 rpm for 60 s, and subsequent thermal annealing at 120 °C for 10 min. Thermal annealing improved the PCE of all devices considerably, especially for the **H14**:IDIC-4F blend. **Figure 2** shows the current density–voltage (J–V) characteristics of SM-OSCs using as-cast and thermally annealed blends. The corresponding photovoltaic parameters are summarized in **Table 1**.
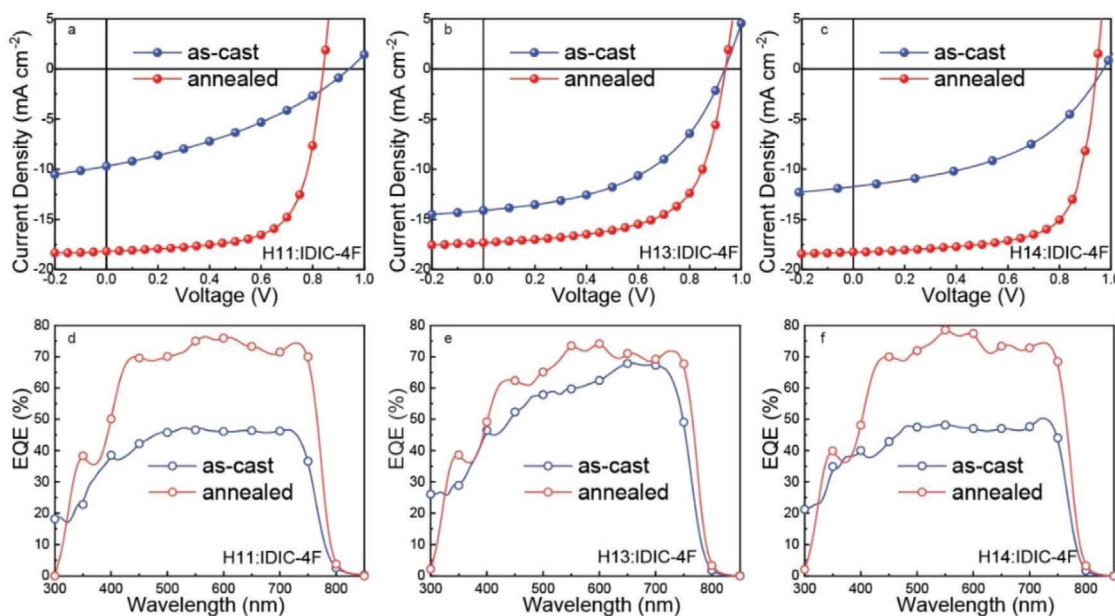
Figure 2. a–c) J–V characteristics of as-cast and thermally annealed SM-OSCs based on **H11**, **H13**, and **H14** as donor and IDIC-4F as acceptor, measured under simulated AM1.5G (100 mW cm^{-2}) illumination. d–f) Corresponding EQE spectra.

As-cast **H13**:IDIC-4F devices displayed a PCE of 6.4%, while **H11** and **H14**-based SM-OSCs exhibited lower PCEs, down to only 3.2% for **H11**. Upon thermal annealing of the blends, the PCE of **H11**-based solar cells increased significantly to 10.4%, with V_{oc} = 0.842 V, J_{sc} = 18.2 mA cm^{-2}, and FF = 68.2%. Thermally annealed **H13**-based cells also showed an improved PCE of 10.3%, with V_{oc} = 0.939 V, J_{sc} = 17.3 mA cm^{-2}, and FF = 63.2%. Finally, cells based on **H14** as donor reached the highest PCE of 12.1% after annealing, featuring high V_{oc} = 0.943 V, high J_{sc} = 18.3 mA cm^{-2}, and high FF = 70.2%. Hence, while the introduction of F atoms in **H13** improves the V_{oc} via a lower HOMO energy, the J_{sc} and FF after annealing are lower than for **H11**-based devices. Introducing Cl atoms in **H14**, however, improves all three parameters, V_{oc}, J_{sc}, and FF simultaneously. The different increase in PCE after thermal annealing of IDIC-4F blends with donor molecules carrying either H, F, or Cl atoms on the side chains is due to a different evolution of the phase morphology and is discussed subsequently.

To ascertain the origin of the changes in J_{sc}, external quantum efficiency (EQE) spectra of the as-cast and annealed SM-OSCs were measured (Figure 2d–f). All thermally annealed blends exhibit a higher EQE in the 300–800 nm

wavelength range than as-cast devices. The increase is especially prominent for the **H11** and **H14**-based devices, while the **H13**-based device shows a much smaller increase. The J_{sc} values integrated from the EQE spectra are listed in Table 1 and are mostly within 2% mismatch with the values obtained from the J–V curves.

To understand why thermal annealing improves the photovoltaic performance of the SM-OSCs, we first investigated the exciton dissociation and charge collection properties of the as-cast and thermally annealed SM-OSCs by measuring the dependence of the photocurrent density (J_{ph}) on the effective voltage (V_{eff}). **Figure 3**a–c shows the photocurrent density (J_{ph}) versus the effective voltage (V_{eff}) of as-cast and thermally annealed SM-OSCs. J_{ph} was determined from $J_{ph} = J_L - J_D$, where J_L is the photocurrent density under illumination and J_D is the dark current density. The effective voltage is defined as $V_{eff} = V_0 - V_{bias}$, where V_0 and V_{bias} are the voltages at which J_{ph} is zero and the applied external voltage bias, respectively. The charge collection probability (P_{cc}) can be estimated from J_{ph} divided by J_{sat} (saturated photocurrent density). At the maximum power point, the P_{cc} values of the as-cast and thermally annealed SM-OSC devices calculated from the results

Table 1. Photovoltaic parameters of the SM-OSCs under simulated AM1.5G (100 mW cm^{-2}) illumination.

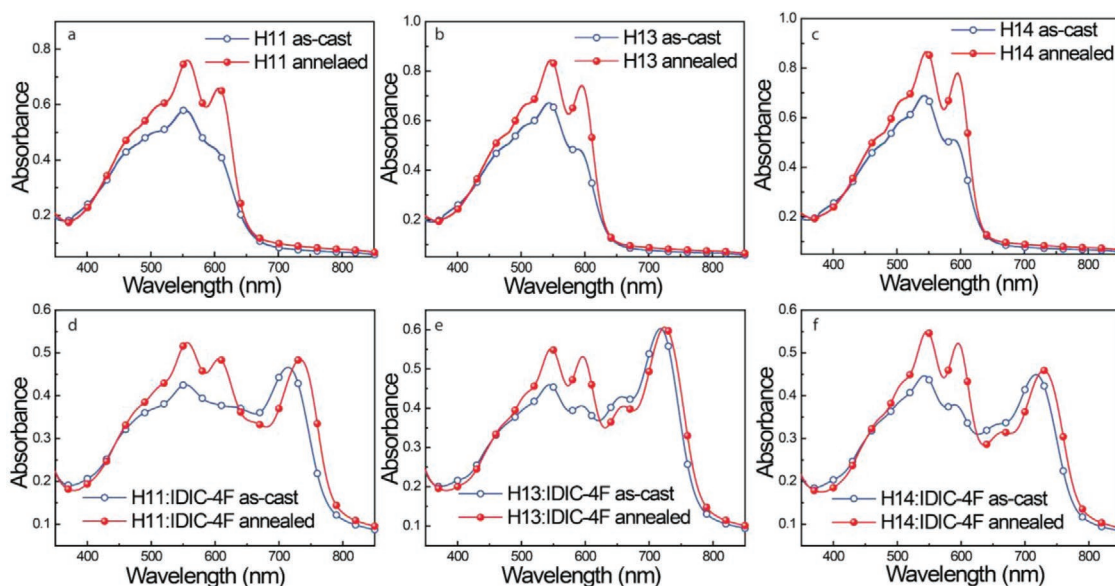| Blend	J_{sc} [mA cm^{-2}]	V_{oc} [V]	FF [%]	PCE [%]	J_{sc}^{EQE} [mA cm^{-2}]	PCE^{EQE} [%]
H11:IDIC-4F[a]	9.7	0.940	35.0	3.2	11.1	3.7
H11:IDIC-4F[b]	18.2	0.842	68.2	10.4	17.9	10.3
H13:IDIC-4F[a]	14.1	0.940	49.0	6.4	14.8	6.8
H13:IDIC-4F[b]	17.3	0.939	63.2	10.3	17.1	10.1
H14:IDIC-4F[a]	11.7	0.975	46.0	5.2	11.6	5.2
H14:IDIC-4F[b]	18.3	0.943	70.2	12.1	18.0	12.0

[a]As-cast devices; [b]Thermally annealed devices.
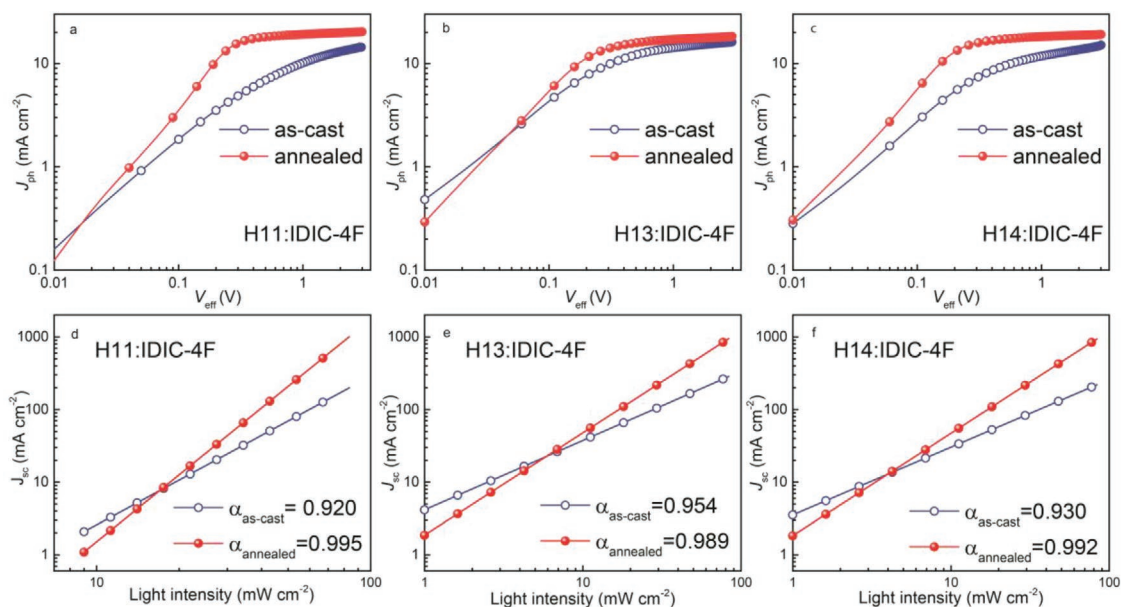
Figure 3. a–c) J_{ph} versus V_{eff} curves of as-cast and thermally annealed devices. d–f) Light intensity dependence of J_{sc}.

in Figure 3a–c are 40.7% and 80.2% for **H11**, 62.4% and 74.6% for **H13**, and 55.3% and 79.8% for **H14**, respectively. These results indicate that thermal annealing significantly improves the charge collection probability and possibly also enhances the charge generation efficiency because also J_{sat} seems to be increased. For the as-cast SM-OSCs, the **H13**-based device shows the highest charge collection efficiency, but among the thermally-annealed SM-OSCs, **H11** and **H14**-based devices show higher charge collection efficiencies. These results clearly demonstrate that in as-cast blends with IDIC-4F, the collection of charges is more efficient with **H13** as donor than with **H11** or **H14**, but that the charge collection efficiency is reversed after thermal annealing, with **H11** and **H14** being better than **H13**.

Since the phase morphology can influence charge extraction and charge recombination, we studied the latter in the as-cast and thermally annealed SM-OSCs by measuring the dependence of J_{sc} on light intensity (P_{light}). J_{sc} and light intensity follow the relation $J_{sc} \propto P_{light}^{\alpha}$, where $\alpha = 1$, if there is no or negligible bimolecular recombination.[33] The plots of log J_{sc} versus log P_{light} are shown in Figure 3d–f. The α values of as-cast and thermally-annealed SM-OSCs are 0.920 and 0.995 for **H11**, 0.954 and 0.989 for **H13**, and 0.930 and 0.992 for **H14** based devices, respectively. These results indicate that thermal annealing suppresses bimolecular recombination, consistent with the increased charge collection extraction efficiency P_{cc}. Furthermore, the α values for the annealed **H11** and **H14**-based SM-OSCs are very close to 1, implying almost no bimolecular recombination at short circuit for these two devices. However, the lower α for **H13**-based device suggests some bimolecular recombination, leading to a lower FF and J_{sc} in the annealed **H13**-based SM-OSCs. For the as-cast SM-OSCs, the α value of **H13** based device is largest, this corresponds to its photovoltaic performance and charge collection efficiency. In addition, we measured the dependence of V_{oc} on light intensity to study the recombination mechanism in these SM-OSCs. Figure S4 (Supporting Information) shows the V_{oc} as function of photon

flux. When trap-assisted recombination is weak, the slope of V_{oc} versus natural logarithm of photon flux should be close to kT/q (where k is the Boltzmann constant, T is the absolute temperature, and q is the elementary charge). Figure S4 (Supporting Information) reveals that slopes of as-cast and thermally-annealed SM-OSCs are 1.17 and 1.30 kT/q for **H11**, 1.04 and 1.29 kT/q for **H13**, and 0.91 and 1.20 kT/q for **H14** based devices, respectively. These results demonstrate that in all blends, the trap-assisted recombination is weak and that bimolecular recombination or surface recombination dominate.

To investigate the charge transport properties, mobilities were determined from the space charge-limited current in the blends using electron-only (ITO/ZnO/active layer/ PDINO/Al) and hole-only (ITO/PEDOT:PSS/active layer/MoO₃/Ag) devices. Figure S5 and Table S9 (Supporting Information) present the measurements and the electron (μ_e) and hole (μ_h) mobilities. In the as-cast devices, **H13**-based devices show the highest μ_e and μ_h of 1.90×10^{-4} and 1.18×10^{-4} cm² V⁻¹ s⁻¹ with $\mu_e/\mu_h = 1.61$. For the **H11** and **H14**-based devices, both μ_e and μ_h are smaller than with **H13**. Especially the low μ_h for **H11** and **H14** causes an unbalanced carrier mobility that leads to a lower FF in the as-cast SM-OSCs. After thermal annealing, all mobilities increased and the charge transport became more balanced (i.e., μ_e/μ_h close to unity). This contributes to the reduced charge recombination, higher FF, and higher J_{sc} in the corresponding SM-OSCs. The **H14**-based device presents the highest μ_e and μ_h of 3.65×10^{-4} and 4.61×10^{-4} cm² V⁻¹ s⁻¹. Compared to the as-cast device both μ_e and μ_h show significant improvements for annealed **H11** and **H14**-based blends. For the **H13**-based devices, the degree of improvement is smaller, with especially μ_e only slightly improved. Because charge transport is directly affected by the nanoscale phase separation and by the molecular packing of the donor and acceptor, the cause for the different extent of improvement induced by the thermal annealing can be a difference in phase separation and/or molecular packing in the active layers.

**ADVANCED
SCIENCE NEWS**

www.advancedsciencenews.com
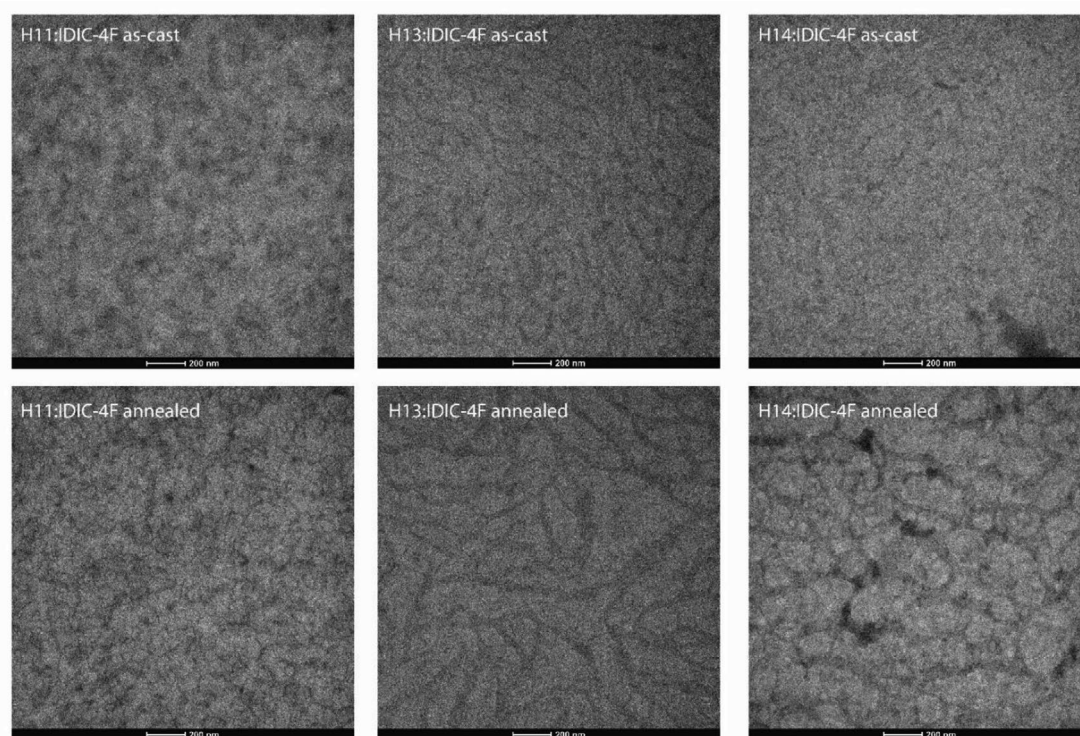
**ADVANCED
ENERGY
MATERIALS**

www.advenergymat.de

Figure 4. a–c) Absorption spectra of neat donor films without/with thermal annealing. d–f) Absorption spectra of blend films without/with thermal annealing.

The optical properties of molecular materials generally depend on intermolecular interactions and hence crystal structure. Absorption spectroscopy can be used to identify the extent of the intermolecular ordering before and after thermal annealing. The optical absorption spectra shown in **Figure 4** reveal that for all neat donor films, the absorbance increased with thermal annealing, also giving rise to more distinct shoulders and peaks. There is no real redshift, so the increased absorbance might be dominated by orientational effects. Alternatively, thermal annealing might increase the density (due to closer packing), increasing the refractive index and thus increasing reflection. We also measured the neat-film absorption spectrum of the IDIC-4F acceptor (Figure S6, Supporting Information) before and after thermal annealing and found a small increase in optical density for the latter. In blends with IDIC-4F, **H11** and **H14** show the same tendency as in the neat films, i.e., the optical densities increase significantly. Thermal annealing also causes a small redshift and increased optical density for IDIC-4F in the blends. These changes imply that in **H11** and **H14**-based blends, the donor and acceptor molecules rearrange either by increasing their intermolecular order or by reorientation. For the **H13**-based blend film, the optical density in the range of 500–630 nm increased less upon annealing and the optical density of the acceptor actually increased negligibly, while its absorption maximum showed a smaller redshift than in the other two blends. We found the same minor change when annealing a 2:1 **H13**:IDIC-4F blend. These results suggest that thermal annealing does not affect the molecular packing of **H13**:IDIC-4F blends significantly. We do point out that while the changes are small, the spectrum of IDIC-4F in the **H13** blend film has strongest optical density of all films (the thickness are all 85 nm) after thermal annealing.

The phase separation of these three BHJ films induced by casting and subsequent thermal annealing was then studied in more detail. First, the surface morphologies of the neat and blend films without/with thermal annealing were investigated by atomic force microscopy (AFM) in tapping-mode. Figure S7 (Supporting Information) shows that the neat films of the three donors exhibit very similar surface morphologies. A more textured surface and larger aggregates can be seen after thermal annealing and the root-mean-squared surface roughness (R_q) increases accordingly. This endorses the conclusion from the optical absorption spectra that thermal annealing affects the film morphology. IDIC-4F has a much higher R_q, suggesting that its coplanar structure leads to strong self-aggregation, which is enhanced by thermal annealing. Figure S8 (Supporting Information) shows the AFM height images of the blend films without/with thermal annealing. For **H11** and **H14**-based blend films, R_q increases and more textured surfaces can be observed after thermal annealing, suggesting that the aggregation of the blend films is improved. In contrast, for **H13**-based films, the as-cast blends already have a large surface roughness and the domain size does and surface roughness do not increase after thermal annealing. Again this was found to be independent of whether the weight ratio H13:IDIC-4F was 1.5:1 or 2:1. This suggests stronger and more pronounced self-aggregation in as-cast blends of **H13** with IDIC-4F, than in **H11** and **H14**-based blends. From the notable surface roughness that changes only little after the thermal annealing, we infer that in the as-cast blend **H13** and IDIC-4F have aggregated already and that thermal annealing does not enhance it significantly. We also studied the as-cast and annealed BHJ films morphology with transmission electron microscopy (TEM). TEM shows little contrast for each of the three blends in the as-cast films (**Figure 5**). After thermal annealing significant modulation appears on a length scale larger than the thickness (85 nm) of the films.

It is relevant to comment on the changes in V_{oc} before and after annealing. As shown, thermal annealing changes the aggregation behavior of the donor/acceptor and thus influences

**ADVANCED
SCIENCE NEWS**
www.advancedsciencenews.com

**ADVANCED
ENERGY
MATERIALS**
www.advenergymat.de

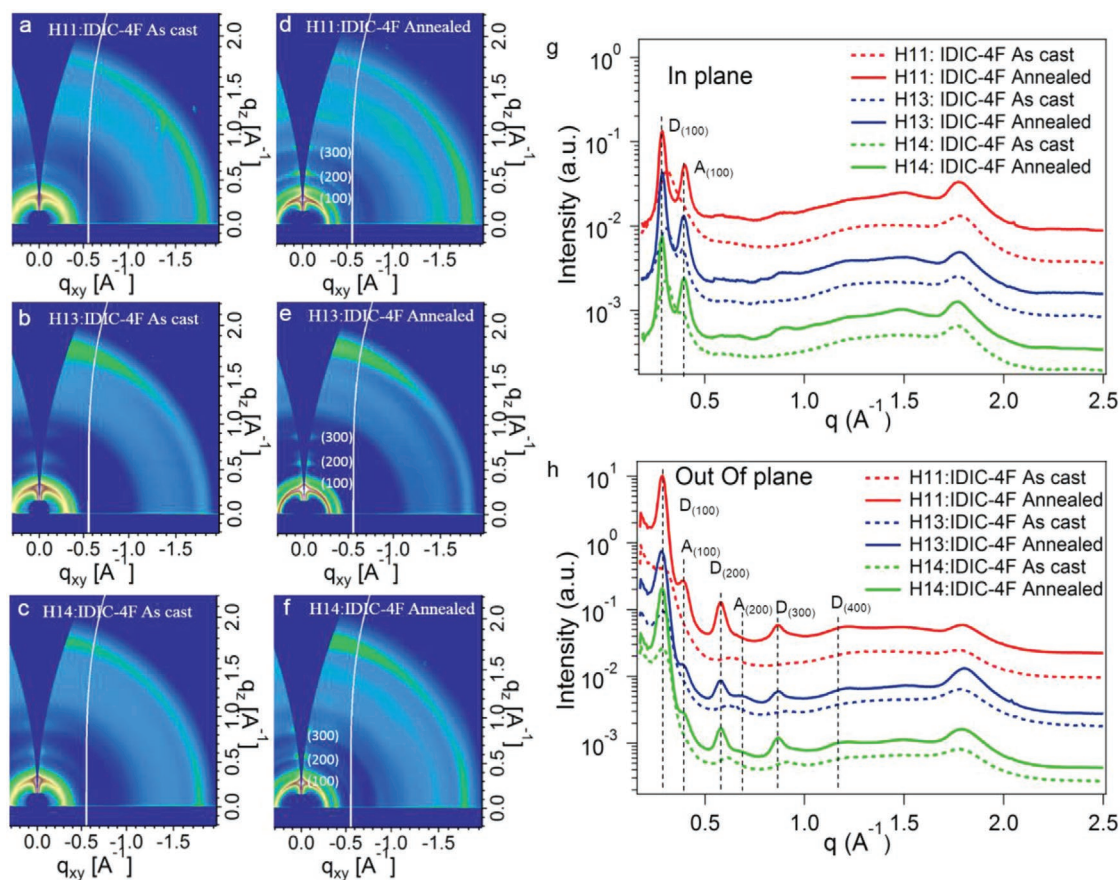**Figure 5.** TEM images of the three blends without and with thermal annealing.

the energy positions. For the three blends studied here, the most obvious change in aggregation due to thermal annealing is for **H11**:IDIC-4F, followed by **H14**:IDIC-4F, while for **H13**:IDIC-4F there is little significant change. This corresponds to the changes in V_{oc} in these systems (**H11**: 0.94 → 0.84 V, **H13**: 0.94 → 0.94 V, and **H14**: 0.98 → 0.94 V). The different changes in energy levels are also seen in absorption spectra of the blends. The **H13**-based film shows the smallest redshift and has the smallest change in V_{oc}, while for the **H11**-based film the largest redshift and the largest change in V_{oc} occur upon annealing.

For deeper understanding of the molecular packing and crystallinity, the neat films and the blend films were studied by grazing-incidence wide-angle X-ray scattering (GIWAXS).[34] Figure S9 (Supporting Information) shows the 2D GIWAXS patterns of the neat films of **H11**, **H13**, and **H14** with and without thermal annealing. Both the as-cast and thermally-annealed donor films exhibit an in-plane (IP) π–π stacking peak (010) at ≈1.77 Å^{-1} in combination with a progression of lamellar (h00) stacking peaks at ≈0.3 Å^{-1} (for h = 1) in the out-of-plane (OOP) direction, indicating that the donors prefer an edge-on orientation. The integrated peak intensity increases with annealing (Table S10, Supporting Information) and more intense diffraction peaks due to lamellar stacking in OOP and π–π stacking in IP directions are observed. This confirms that thermal annealing promotes aggregation and enhances the edge-on orientation of the neat donors. In contrast, the coherence length of the π–π stacking is virtually unchanged with a g-parameter[35–37] around 10%, indicating uniform paracrystallinity for all materials and conditions (Table S10, Supporting Information) and the presence of small aggregates

rather than crystallites. As shown in Figure S10 (Supporting Information), IDIC-4F in as-cast and thermally annealed films show a predominantly face-on orientation with a π–π stacking peak at 1.8 Å^{-1} in OOP direction. With annealing, the π–π stacking distance and the coherence length do not change but the integrated intensity increases somewhat. The lamellar stacking peak becomes more pronounced, indicating a higher degree of overall molecular ordering and aggregation for IDIC-4F after thermal annealing. According to Figure S10 (Supporting Information), IDIC-4F has a g-parameter ≈12% for the (010) peak. Generally, g = 0% indicates a perfect crystal and 0% < g < 2% represents crystalline ordering, while 2% < g < 12% is paracrystalline ordering. Amorphous silicon dioxide g parameter is ≈12%; therefore g > 12% is referred to the amorphous ordering.[38] Hence, IDIC-4F is largely amorphous along the π–π direction.

Figure 6 shows the 2D GIWAXS patterns of the blend films and the corresponding IP and OOP direction line cuts. It can be readily observed from the more pronounced peaks that annealing improves the molecular packing, particularly of the acceptor. **H11** and **H14**-based blends have stronger (100) diffraction intensity than **H13**, and in the OOP direction, **H13**-based blends have strongest (010) diffraction intensity, followed by **H14**, and by **H11** which is the weakest. More importantly, after thermal annealing, the lamellar stacking peaks (100), (200), (300), and (400) in the OOP direction of **H11** and **H14**-based blends become more distinct with enhanced diffraction intensities, while the corresponding peaks for **H13**-based blends are only slightly increased. In order to analyze the π–π stacking of donor and IDIC-4F in

**ADVANCED
SCIENCE NEWS**

www.advancedsciencenews.com

**ADVANCED
ENERGY
MATERIALS**

www.advenergymat.de

Figure 6. a–f) 2D GIWAXS patterns and g,h) in-plane and out-of-plane scattering profiles of the blend films without and with thermal annealing. A and D labels in the panels (g) and (h) show the lamellar peaks of the acceptor and the donors, respectively.

the blend films, peak fitting was utilized to assess peak location, intensity, and width, from which distances and coherence length and g-parameters are calculated. As **H11** and IDIC-4F have quite similar π–π stacking peaks and distances, their contribution could not be disentangled. The combined analysis exhibited little change due to annealing (Table S11, Supporting Information). For **H13** and **H14**-based blend films the acceptor and donor can be distinguished, and the results are summarized in Table S12 (Supporting Information). For the **H13**-based blends, the π–π stacking distance of IDIC-4F becomes smaller (from 3.47 to 3.40 Å) after annealing, and the π–π stacking distance (3.51 Å) of **H13** and the coherence lengths of both **H13** (46 Å) and IDIC-4F (25 Å) do not change. In contrast, for the **H14** based blends, both the π–π stacking distance and the coherence length of **H14** and IDIC-4F are improved by annealing. The coherence length of **H14** improved from 40 to 50 Å and for IDIC-4F from 20 to 29 Å. Such an increase in π–π coherence length and corresponding lowering of the associated paracrystalline distortions has been previously linked to improved performance.[25]

In order to assess the degree of crystallinity/aggregation and the texture of the films (edge-on versus face-on orientation and mixed orientations), we carefully analyze pole figures (Figure S11, Supporting Information). Since it was not possible to extract the pole figure of the (010) peaks of acceptor and

donor separately, we utilized the respective (100) peaks to distinguish the acceptor from the donor. Assuming a 2D powder, the donor lamellar (100) pole figure indicates that the donors in all the blends are predominantly edge-on, with **H13** the most isotropic (Figure S11, Supporting Information). In contrast, the IDIC-4F (100) pole figure suggests that the acceptor is highly face-on in **H11** blends and exhibits strong bimodal (edge- and face-on) orientation in **H13** and **H14** blends. Out of these three blends, the **H13** blend has the most pronounced bimodal distribution compared to the other two blends but does not show superior PCE. Although our previous report indicated that mixed edge-on and face-on orientations can enable high efficiency OSCs with 3D pathways for vertical and parallel charge transport in BHJ films,[24] the lack of clear correlation and difficulty in differentiating the separate impact of the texture of the donor and the texture of the acceptor indicate that texture is not a dominating factor here. In contrast, the relative degree of crystallinity (rDoC)[39] calculated from the (100) peak pole figure shows that in the **H14** blend, both the acceptor and the donor have the highest relative degree of crystallinity (Table S13, Supporting Information), correlating with the superior performance of the **H14** blend.

Out of the six parameters that define the molecular packing, i.e., degree of crystallinity/aggregation, coherence length/g parameter, and texture for the donor and the acceptor separately, the

coherence length and degree of aggregation seem to have the most pronounced impact, particularly of the acceptor. We note that the donor and acceptor impact each other in their molecular packing, which might have thermodynamic or kinetic origins. We will delineate some of the thermodynamic factors, i.e., molecular interactions, below.

Resonant soft X-ray scattering (R-SoXS)[40] is known as an advanced tool to quantify the size distributions of the domains,[41] relative composition variations[42] (monotonically related to "domain purity"), and possibly even molecular orientation.[43] We employed R-SoXS to investigate the phase separation and phase purity of the blend films without/with thermal annealing. According to reported protocols, in multiphase systems, the integrated scattering intensity and the component scattering intensity[44,45] of organic blend films can be used to quantify the variance (σ^2) or standard deviation (σ) of the composition, which is monotonically related to relative domain purity. In many cases, σ correlates linearly with the device FF if there is no loss of charge percolation in the mixed domains.[7,10,32–34,39–40,44–46] Such correlations need to generally consider scattering contrast from orientation distributions and contrast changes if the texture is changing between samples.[42]
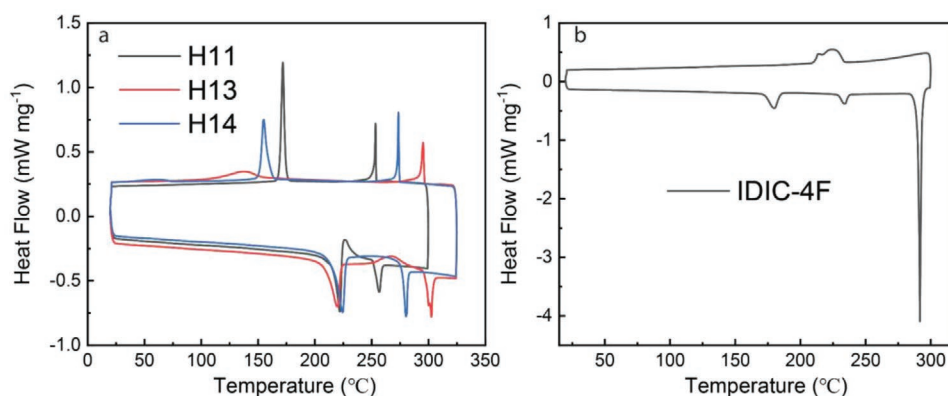
Correlation of the meso-scale morphology to device performance is complicated here by the fact that there is significant modulation on length scales larger than the film thickness of 86 nm, as can be clearly observed from the TEM. This implies that there are possibly two different BHJ morphologies in parallel. The Lorentz corrected R-SoXS profiles (Kratky plot) are

shown in **Figure 7**. The raw data directly indicates a few basic observations and conclusions. The total scattering intensity (the integrated area under the graphs) increases significantly for **H11**:IDIC-4F when annealed, decreases significantly for **H13**:IDIC-4F, and decreases slightly for **H14**:IDIC-4F. Additionally, **H14**:IDIC-4F exhibits significant coarsening. The scattering intensity is impacted by both the volume fraction of the pure phase of each component, as well as the composition of the mixed domains and even orientational distributions. Overall, the observed differences imply differences in the kinetics of film formation and thermodynamics during annealing. The following scenario is the most likely. **H11**:IDIC-4F is a deep quench system (low miscibility, high interaction parameter), and its mixed domains are significantly quenched during casting by an early liquid to solid transition. During annealing the domains purify and aggregate/crystallites form, increasing the scattering intensity. **H13**:IDIC-4F corresponds to a shallow quench (small interaction parameter) with an upper critical solution temperature that is so low that mixing increases and aggregation decreases at 120 °C. **H14**:IDIC-4F has intermediate miscibility, but high molecular mobility that allows for the coarsening of the morphology at larger length scales.

Previously, it was observed that for multilength scale morphology with domains larger as well as smaller than the film thickness, a correlation to device performance could still be established by considering the composition characteristics at the smallest lengths scales.[40] We have therefore performed multipeak lognormal fits of the R-SoXS profiles following previous protocols (see details in Figure S12, Supporting
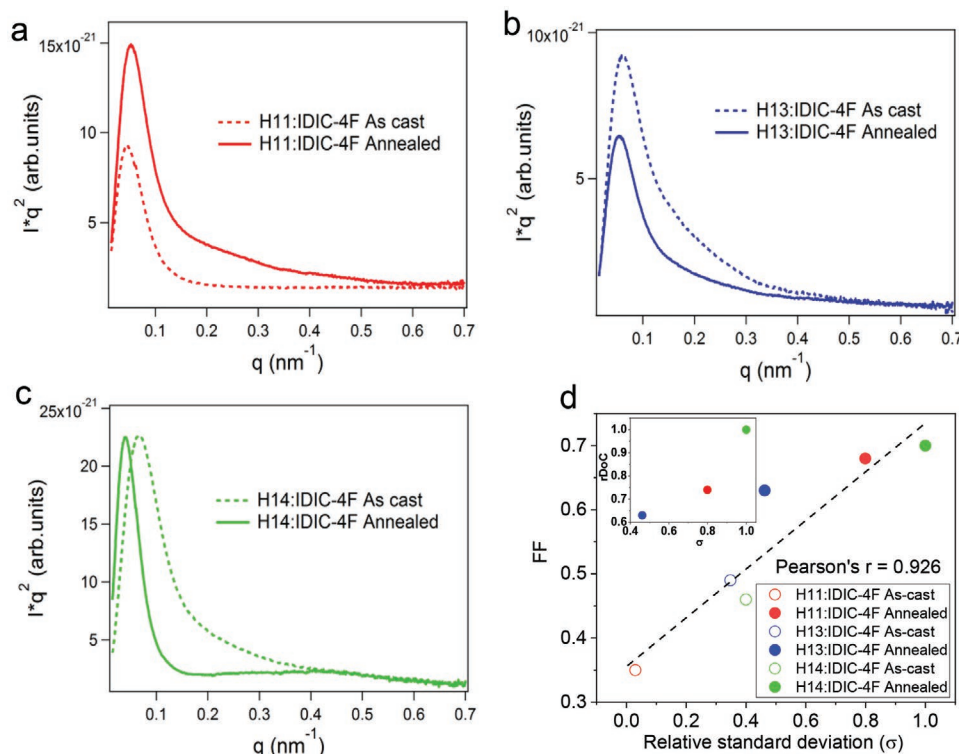
Figure 7. Thickness and absorption normalized and Lorentz corrected R-SoXS profiles obtained at 283.2 eV. a) H11:IDIC-4F. b) H13:IDIC-4F. c) H14:IDIC-4F. d) Correlation of the relative standard deviation (σ) of the composition corresponding to the log-normal distribution of the blends at high q to the FF of all six devices. The inset shows the correlation between σ and the rDoC of the donors of the annealed samples.

ADVANCED
SCIENCE NEWS
www.advancedsciencenews.com

ADVANCED
ENERGY
MATERIALS
www.advenergymat.de

Figure 8. DSC thermograms of a) **H11**, **H13**, **H14** and b) IDIC-4F at a rate of 10 °C min^{-1}, the lower traces are from the heating cycles and upper traces are from the cooling cycles.

Information).[47] As shown in Table S14 (Supporting Information), the standard deviation of the composition of the log-normal distribution corresponding to the highest q increases with thermal annealing for all the blends, suggesting annealed blends have purer domains or more aggregates at small lengths scales. In pure domains, one type of charge carrier is predominantly present and, hence, higher domain purity would result in less bimolecular recombination, yielding a higher FF. Despite our inability to fully normalize out all possible contributions to the scattering intensity from factors other than composition due to some technical challenges, the FF of all six devices correlates with a Pearson coefficient of 0.92 with the standard deviation (σ) of the composition (Figure 7d). The correlations indicate a strong impact of the nanoscale morphology on device performance. We note that σ of the annealed samples correlates with the degree of aggression of the donor (inset to Figure 7d) and that the donor aggregation is thus likely the predominant factor that is driving the morphology development at the small length scale.

To better understand the aggregation and crystallization of the donors at elevated temperature, differential scanning calorimetry (DSC) measurements were performed on powdered samples of **H11**, **H13**, and **H14**. **Figure 8** shows that at slow heating or cooling rate (10 °C min^{-1}), all the donors exhibit two endothermic peaks and two exothermic peaks, respectively, indicating the existence of a mesophase or liquid crystalline phase between the crystalline phase and the melt. DSC measurements on IDIC-4F show three endothermic peaks of which last one at 291 °C is the melting transition. At the melting temperature IDIC-4F decomposes and only a broad exothermic signal is seen in the cooling run and a subsequent heating scan shows an ill-defined peak at ≈275 °C.

A liquid crystalline phase as observed for the donors has been shown in some systems to be beneficial for achieving an ordered molecular packing and efficient charge transport in the active layer.[48] The DSC traces show that upon cooling, the transition from the mesophase to the crystalline phase is not only lower in temperature for **H13**, it is also much broader for **H13** than for **H11** or **H14**. The hampered crystallization of **H13** may explain, in addition to the inferred low critical temperature and shallow quench depth, why it is difficult to improve the phase separation and domain purity of **H13** based blends

with thermal annealing. Kinetics and thermodynamics inhibit further **H13** device optimization. If the total melting enthalpies are also indicative of the relative strength of the amorphous self-interactions of the materials, the DSC data support the low miscibility of the **H11** blend derived from R-SoXS, as a smaller self-interaction generally leads to a smaller χ parameter and lower miscibility.

3. Conclusions

In conclusion, based on the promising donor material **H11**, we designed and synthesized two new small molecule donors, **H13** and **H14**, by introducing F atoms or Cl atoms on the side chains. In combination with IDIC-4F as acceptor, **H11**, **H13**, and **H14** gave high performance SM-OSCs. **H14** based devices present the highest PCEs, up to 12.1%. The chlorinated **H14** donor molecules combine a low-lying HOMO energy level, with strong intermolecular interaction and high degree of aggregation. After thermal annealing the **H14**/IDIC-4F blends reach a phase separation with appropriated aggregated domains at small length scales and with the higher relative purity, leading to efficient charge generation and collection. The low low-lying HOMO of **H14** provides the highest V_{oc} of 0.943 V among the three donors, and the nanoscale phase separation leads to a high EQE between 70% and 80% and a corresponding high J_{sc} of 18.3 mA cm^{-2}, while the optimized pathways for charge collection reduce bimolecular recombination and increase the FF of 70.2%. While the fluorinated **H13** donor also possess a lower HOMO energy than **H11**, resulting in an improved V_{oc}, the morphology of the **H13**-based blends after annealing is inferior compared to **H11** and **H14**-based blends, resulting in lower J_{sc} and FF. In **H13**:IDIC-4F blends some self-aggregation of the donor and acceptor does occurs already in as-cast films; however, the aggregation of **H13** is kinetically and thermodynamically (low miscibility) hindered in the solid state and thermal annealing does not improve aggregation as much as for **H11** and **H14**. In summary, we achieved precise control of the phase separation through molecular design in combination with thermal annealing, and obtained SM-OSCs with a PCE over 12%, which is the highest efficiency for the IDIC-4F-based SM-OSCs.

ADVANCED
SCIENCE NEWS
www.advancedsciencenews.com

ADVANCED
ENERGY
MATERIALS
www.advenergymat.de

Supporting Information

Acknowledgements

Conflict of Interest

The authors declare no conflict of interest.

Keywords

[1] Z. He, B. Xiao, F. Liu, H. Wu, Y. Yang, S. Xiao, C. Wang, T. P. Russell, Y. Cao, *Nat. Photonics* **2015**, *9*, 174.

[2] Y. F. Li, *Acc. Chem. Res.* **2012**, *45*, 723.

[3] J. Hou, O. Inganas, R. H. Friend, F. Gao, *Nat. Mater.* **2018**, *17*, 119.

[4] L. Liu, Y. Kan, K. Gao, J. Wang, M. Zhao, H. Chen, C. Zhao, T. Jiu, A. K. Y. Jen, Y. Li, *Adv. Mater.* **2020**, *32*, 1907604.

[5] Y. Lin, B. Adilbekova, Y. Firdaus, E. Yengel, H. Faber, M. Sajjad, X. Zheng, E. Yarali, A. Seitkhan, O. M. Bakr, A. El-Labban, U. Schwingenschlögl, V. Tung, I. McCulloch, F. Laquai, T. D. Anthopoulos, *Adv. Mater.* **2019**, *31*, 1902965.

[6] L. Zhan, S. Li, T. K. Lau, Y. Cui, X. Lu, M. Shi, C. Z. Li, H. Li, J. Hou, H. Chen, *Energy Environ. Sci.* **2020**, *13*, 635.

[7] Y. Cui, H. Yao, J. Zhang, K. Xian, T. Zhang, L. Hong, Y. Wang, Y. Xu, K. Ma, C. An, C. He, Z. Wei, F. Gao, J. Hou, *Adv. Mater.* **2020**, *32*, 1908205.

[8] C. Yan, S. Barlow, Z. Wang, H. Yan, A. K. Y. Jen, S. R. Marder, X. Zhan, *Nat. Rev. Mater.* **2018**, *3*, 18003.

[9] H. Bin, Z. G. Zhang, L. Gao, S. Chen, L. Zhong, L. Xue, C. Yang, Y. Li, *J. Am. Chem. Soc.* **2016**, *138*, 4657.

[10] W. Zhao, S. Li, H. Yao, S. Zhang, Y. Zhang, B. Yang, J. Hou, *J. Am. Chem. Soc.* **2017**, *139*, 7148.

[11] H. Bin, L. Gao, Z. G. Zhang, Y. Yang, Y. Zhang, C. Zhang, S. Chen, L. Xue, C. Yang, M. Xiao, Y. Li, *Nat. Commun.* **2016**, *7*, 13651.

[12] L. Ye, H. Hu, M. Ghasemi, T. Wang, B. A. Collins, J. H. Kim, K. Jiang, J. H. Carpenter, H. Li, Z. Li, T. McAfee, J. Zhao, X. Chen, J. L. Y. Lai, T. Ma, J. L. Bredas, H. Yan, H. Ade, *Nat. Mater.* **2018**, *17*, 253.

[13] L. Ye, S. Li, X. Liu, S. Zhang, M. Ghasemi, Y. Xiong, J. Hou, H. Ade, *Joule* **2019**, *3*, 443.

[14] L. Ye, X. Jiao, S. Zhang, H. Yao, Y. Qin, H. Ade, J. Hou, *Adv. Energy Mater.* **2017**, *7*, 1601138.

[15] W. Ma, G. Yang, K. Jiang, J. H. Carpenter, Y. Wu, X. Meng, T. McAfee, J. Zhao, C. Zhu, C. Wang, H. Ade, H. Yan, *Adv. Energy Mater.* **2015**, *5*, 1501400.

[16] D. Hu, Q. Yang, H. Chen, F. Wobben, V. M. Le Corre, R. Singh, T. Liu, R. Ma, H. Tang, L. J. A. Koster, T. Duan, H. Yan, Z. Kan, Z. Xiao, S. Lu, *Energy Environ. Sci.* **2020**, *13*, 2134.

[17] H. Chen, D. Hu, Q. Yang, J. Gao, J. Fu, K. Yang, H. He, S. Chen, Z. Kan, T. Duan, C. Yang, J. Ouyang, Z. Xiao, K. Sun, S. Lu, *Joule* **2019**, *3*, 3034.

[18] K. Gao, S. B. Jo, X. Shi, L. Nian, M. Zhang, Y. Kan, F. Lin, B. Kan, B. Xu, Q. Rong, L. Shui, F. Liu, X. Peng, G. Zhou, Y. Cao, A. K. Y. Jen, *Adv. Mater.* **2019**, *31*, 1807842.

[19] H. Bin, J. Yao, Y. Yang, I. Angunawela, C. Sun, L. Gao, L. Ye, B. Qiu, L. Xue, C. Zhu, C. Yang, Z. G. Zhang, H. Ade, Y. Li, *Adv. Mater.* **2018**, *30*, 1706361.

[20] Q. Burlingame, X. Huang, X. Liu, C. Jeong, C. Coburn, S. R. Forrest, *Nature* **2019**, *573*, 394.

[21] Y. Li, H. K. M. Sheriff, X. Liu, C. K. Wang, K. Ding, H. Han, K. T. Wong, S. R. Forrest, *J. Am. Chem. Soc.* **2019**, *141*, 18204.

[22] X. Dong, K. Yang, H. Tang, D. Hu, S. Chen, J. Zhang, Z. Kan, T. Duan, C. Hu, X. Dai, Z. Xiao, K. Sun, S. Lu, *Sol. RRL* **2020**, *4*, 1900326.

[23] Q. Yue, H. Wu, Z. Zhou, M. Zhang, F. Liu, X. Zhu, *Adv. Mater.* **2019**, *31*, 1904283.

[24] H. Bin, Y. Yang, Z. G. Zhang, L. Ye, M. Ghasemi, S. Chen, Y. Zhang, C. Zhang, C. Sun, L. Xue, C. Yang, H. Ade, Y. Li, *J. Am. Chem. Soc.* **2017**, *139*, 5085.

[25] H. Hu, K. Jiang, P. C. Y. Chow, L. Ye, G. Zhang, Z. Li, J. H. Carpenter, H. Ade, H. Yan, *Adv. Energy Mater.* **2018**, *8*, 1601138.

[26] L. Zhu, W. Zhong, C. Qiu, B. Lyu, Z. Zhou, M. Zhang, J. Song, J. Xu, J. Wang, J. Ali, W. Feng, Z. Shi, X. Gu, L. Ying, Y. Zhang, F. Liu, *Adv. Mater.* **2019**, *31*, 1902899.

[27] J. Yuan, Y. Zhang, L. Zhou, G. Zhang, H. L. Yip, T. K. Lau, X. Lu, C. Zhu, H. Peng, P. A. Johnson, M. Leclerc, Y. Cao, J. Ulanski, Y. Li, Y. Zou, *Joule* **2019**, *3*, 1140.

[28] S. Zhang, Y. Qin, J. Zhu, J. Hou, *Adv. Mater.* **2018**, *30*, 1800868.

[29] H. Chen, Z. Hu, H. Wang, L. Liu, P. Chao, J. Qu, W. Chen, A. Liu, F. He, *Joule* **2018**, *2*, 1623.

[30] Z. Liu, Y. Gao, J. Dong, M. Yang, M. Liu, Y. Zhang, J. Wen, H. Ma, X. Gao, W. Chen, M. Shao, *J. Phys. Chem. Lett.* **2018**, *9*, 6955.

[31] S. Li, L. Ye, W. Zhao, H. Yan, B. Yang, D. Liu, W. Li, H. Ade, J. Hou, *J. Am. Chem. Soc.* **2018**, *140*, 7159.

[32] H. Li, Q. Wu, R. Zhou, Y. Shi, C. Yang, Y. Zhang, J. Zhang, W. Zou, D. Deng, K. Lu, Z. Wei, *Adv. Energy Mater.* **2019**, *9*, 1803175.

[33] A. K. K. Kyaw, D. H. Wang, V. Gupta, W. L. Leong, L. Ke, G. C. Bazan, A. J. Heeger, *ACS Nano* **2013**, *7*, 4569.

[34] A. Hexemer, W. Bras, J. Glossinger, E. Schaible, E. Gann, R. Kirian, A. MacDowell, M. Church, B. Rude, H. Padmore, *J. Phys.: Conf. Ser.* **2010**, *247*, 012007.

[35] A. M. Hindeleh, R. Hosemann, *J. Mater. Sci.* **1991**, *26*, 5127.

[36] R. Noriega, J. Rivnay, K. Vandewal, F. P. V. Koch, N. Stingelin, P. Smith, M. F. Toney, A. Salleo, *Nat. Mater.* **2013**, *12*, 1038.

[37] B. I. Yavuz, B. N. Martin, J. Park, K. N. Houk, *J. Am. Chem. Soc.* **2015**, *137*, 2856.

[38] J. Rivnay, R. Noriega, R. J. Kline, A. Salleo, M. F. Toney, *Phys. Rev. B* **2011**, *84*, 045203.

[39] B. W. Boudouris, V. Ho, L. H. Jimison, M. F. Toney, A. Salleo, R. A. Segalman, *Macromolecules* **2011**, *44*, 6653.

[40] E. Gann, A. T. Young, B. A. Collins, H. Yan, J. Nasiatka, H. A. Padmore, H. Ade, A. Hexemer, C. Wang, *Rev. Sci. Instrum.* **2012**, *83*, 045110.

[41] B. A. Collins, Z. Li, J. R. Tumbleston, E. Gann, C. R. Mcneill, H. Ade, *Adv. Energy Mater.* **2013**, *3*, 65.

[42] S. Mukherjee, C. M. Proctor, J. R. Tumbleston, G. C. Bazan, T. Q. Nguyen, H. Ade, *Adv. Mater.* **2015**, *27*, 1105.

[43] J. R. Tumbleston, B. A. Collins, L. Yang, A. C. Stuart, E. Gann, W. Ma, W. You, H. Ade, *Nat. Photonics* **2014**, *8*, 385.

[44] S. Mukherjee, X. Jiao, H. Ade, *Adv. Energy Mater.* **2016**, *6*, 1600699.

[45] S. Mukherjee, C. M. Proctor, G. C. Bazan, T. Q. Nguyen, H. Ade, *Adv. Energy Mater.* **2015**, *5*, 1500877.

[46] I. Angunawela, L. Ye, H. Bin, Z. G. Zhang, A. Gadisa, Y. Li, H. Ade, *Mater. Chem. Front.* **2019**, *3*, 137.

[47] N Stribeck. *X-Ray Scattering of Soft Matter*, Springer Science & Business Media, Berlin **2007**.

[48] K. Sun, Z. Xiao, S. Lu, W. Zajaczkowski, W. Pisula, E. Hanssen, J. M. White, R. M. Williamson, J. Subbiah, J. Ouyang, A. B. Holmes, W. W. H. Wong, D. J. Jones, *Nat. Commun.* **2015**, *6*, 6013.

2001589 (12 of 12)